RSC Advances

PAPER

View Article Online
View Journal | View Issue

Cite this: RSC Adv., 2017, 7, 13331

Hydrothermal crystallization of a $Ln_2(OH)_4SO_4 \cdot nH_2O$ layered compound for a wide range of Ln (Ln = La–Dy), thermolysis, and facile transformation into oxysulfate and oxysulfide phosphors†

Xuejiao Wang,[abcd] Ji-Guang Li,*[abc] Maxim S. Molokeev,[ef] Xiaojun Wang,[g] Weigang Liu,[ab] Qi Zhu,[ab] Hidehiko Tanaka,[h] Keiko Suzuta,[h] Byung-Nam Kim[c] and Yoshio Sakka[c]

The synthesis of a layered $Ln_2(OH)_4SO_4 \cdot nH_2O$ material (Ln-241) with a smaller lanthanide ion (Dy^{3+}) was successfully achieved through the optimization of the hydrothermal conditions, and the effect of lanthanide contraction on the chemical composition, phase structure, and crystallite/particle morphology of the products was investigated and discussed. Structure refinement showed that the lattice parameters (*a*, *b*, and *c*), cell volume, and axis angle across the series (Ln = La–Dy) monotonously decrease as the size of Ln^{3+} decreases. Comparative TG/DTA analysis in air indicated that the dehydroxylation temperature of Ln-241 tends to increase, whereas the dehydration and desulfurization temperatures decrease as the size of Ln^{3+} decreases, thus narrowing the stable temperature range for $Ln_2O_2SO_4$. Taking advantage of the fact that Ln-241 has exactly the same Ln/S molar ratio as $Ln_2O_2SO_4$ and Ln_2O_2S, the latter two groups of important compounds (excluding Ce) were facilely transformed from the former *via* the removal of water by calcination. The photoluminescence properties of Eu^{3+} and Tb^{3+}, in terms of excitation, emission, fluorescence decay, quantum yield, and emission color, were investigated and compared for the two hosts Gd_2O_2S and $Gd_2O_2SO_4$, and the $(Gd_{0.99}Tb_{0.01})_2O_2S$ phosphor was shown to be stable under electron beam irradiation in the studied range and exhibited an increasingly higher emission brightness as the acceleration voltage (up to 7 kV) or beam current (up to 50 μA) increased.

Received 16th January 2017
Accepted 12th February 2017

DOI: 10.1039/c7ra00645d

rsc.li/rsc-advances

Introduction

The general chemical formula of layered rare-earth hydroxides (LRHs) can be expressed as $Ln_2(OH)_{6-m}(A^{x-})_{m/x} \cdot nH_2O$ (Ln: trivalent rare-earth ions; A: guest anion; $1.0 \leq m \leq 2.0$),[1,2] with $Ln_2(OH)_5(A^{x-})_{1/x} \cdot nH_2O$ ($m = 1$), termed as the 251 phase, and $Ln_2(OH)_4(A^{x-})_{2/x} \cdot nH_2O$ ($m = 2$), termed as the 241 phase, being two important groups of the family. The 251 phase has drawn significant attention since its first report in 2006 and is finding potential applications in various fields including pollutant trapping, rechargeable batteries, drug delivery, heterogeneous catalysis, and microelectronics.[3–7] The superior performance of Ln-251 motivated researchers to explore LRHs with new compositions. In 2010, the Ln-241 compounds of $Ln_2(OH)_4SO_4 \cdot nH_2O$ (Ln = Pr–Tb) were obtained as a new family of LRH *via* the homogeneous hydrolysis of Ln-sulfate in the presence of hexamethylenetetramine (HMT).[1] Later, in 2011, the crystal structure of Ln-241 was explored for the currently obtainable Pr–Tb analogues.[8] Very recently, the binary $(Ce,Tb)_2(OH)_4SO_4 \cdot nH_2O$ compound was synthesized and an enhanced Tb^{3+} emission was achieved due to efficient energy transfer from Ce^{3+} to Tb^{3+}.[9] However, the Ln-241 phase is yet confined to limited members of Ln and its synthesis is mainly restricted to homogeneous precipitation under ambient pressure. The thus produced Ln-241 materials typically consist of aggregates of

[a]Key Laboratory for Anisotropy and Texture of Materials (Ministry of Education), Northeastern University, Shenyang, Liaoning 110819, China
[b]Institute of Ceramics and Powder Metallurgy, School of Materials Science and Engineering, Northeastern University, Shenyang, Liaoning 110819, China
[c]Research Centre for Functional Materials, National Institute for Materials Science, Tsukuba, Ibaraki 305-0044, Japan. E-mail: LI.Jiguang@nims.go.jp; Tel: +81-29-860-4394
[d]College of New Energy, Bohai University, Jinzhou, Liaoning 121000, China
[e]Laboratory of Crystal Physics, Kirensky Institute of Physics, Federal Research Center KSC SB RAS, Krasnoyarsk 660036, Russia
[f]Department of Physics, Far Eastern State Transport University, Khabarovsk 680021, Russia
[g]School of Physics and Electronic Engineering, Jiangsu Normal University, Xuzhou, Jiangsu 221116, China
[h]World Premier International Centre for Materials Nanoarchitectonics (WPI-MANA), National Institute for Materials Science, Tsukuba, Ibaraki 305-0044, Japan

† Electronic supplementary information (ESI) available. See DOI: 10.1039/c7ra00645d

thin flakes. Therefore, it is highly important to explore other routes for the synthesis of $Ln_2(OH)_4SO_4 \cdot nH_2O$ with a well-controlled morphology and for a wider range of Ln. The behavior of Ln varies in various aspects due to lanthanide contraction;[10,11] hence, it is scientifically fascinating and practically required to establish specific conditions for the synthesis of Ln-241 compounds of different Ln.

Recently, $Ln_2O_2SO_4$ oxysulfates are attracting significant interest in various fields as oxygen storage materials,[12] catalysts for water–gas shift (WGS)[13] and reverse WGS,[14] solid electrolytes,[15] cathodes for solid oxide fuel cells,[16] and in down-/up-conversion luminescence.[17,18] Research, however, has only been limited to a few members of the Ln group (particularly, Gd and Y), and the stable temperature window for $Ln_2O_2SO_4$ compounds is not well established although it was reported that $Lu_2O_2SO_4$ is unstable at room temperature;[19,20] $La_2O_2SO_4$ is stable in air at temperatures as high as 1200 °C.[21] On the other hand, Ln_2O_2S oxysulfides are known as an important group of compounds that are finding practical applications in solid-state lasers, medical X-ray CT, safety indications, and luminescence and display.[22–24] However, their synthesis inevitably involves environmentally harmful sulfur-containing reagents and complicated procedures, either *via* solid-phase reactions[25–27] or wet-chemical synthesis such as the solvothermal pressure-relief process,[28] complex homogeneous precipitation,[29] and one-pot solvothermal reactions.[23] The chemical composition of $Ln_2(OH)_4SO_4 \cdot nH_2O$ compounds provides new opportunities to address the abovementioned challenging issues since these compounds have exactly the same Ln/S molar ratio as Ln_2O_2S and $Ln_2O_2SO_4$ and can thus act as an ideal precursor for the latter two groups of compounds.

In this study, the hydrothermal synthesis of $Ln_2(OH)_4SO_4 \cdot nH_2O$ was conducted for the entire range of Ln (La–Lu), and the effect of lanthanide contraction on the chemical composition, phase structure, and particle morphology were investigated. By adjusting the solution pH, Ln-241 was obtained for the first time for a smaller Ln^{3+} ion, Dy^{3+}, whose structural parameters were also characterized. Thermal decomposition of the compounds in air was studied in detail for each Ln *via* TG/DTA, and the stable temperature window of $Ln_2O_2SO_4$ was well established for Ln = La–Dy. Furthermore, on simply removing water from the Ln-241 precursor *via* calcination in the presence of hydrogen, the Ln_2O_2S compounds were successfully produced. The luminescence properties including excitation, emission, fluorescence decay, quantum yield, and CIE chromaticity of the two important activators Eu^{3+} and Tb^{3+} were also studied with $Gd_2O_2SO_4$ and Gd_2O_2S as the host lattices.

Experimental

Materials and synthesis

The starting materials were $Ln(NO)_3 \cdot 6H_2O$ (Ln = La–Ho, 99.99% pure), Ln_2O_3 (Ln = Er–Lu, 99.99% pure), $(NH_4)_2SO_4$ (>99.5% pure), and $NH_3 \cdot H_2O$ (ultrahigh purity). All chemicals were purchased from Kanto Chemical Co., Inc. (Tokyo, Japan) and were used without further purification. Ln oxide was dissolved using a slight excess of hot nitric acid to prepare the corresponding nitrate solution and superfluous acid was removed by evaporation of the solution at ~90 °C. In a typical synthesis, 0.8 g of $(NH_4)_2SO_4$ (6 mmol) was dissolved in 60 mL of $Ln(NO)_3$ solution (0.1 M), followed by the dropwise addition of $NH_3 \cdot H_2O$ to adjust the solution pH. The resultant turbid solution was transferred to an autoclave (100 mL capacity) after 15 min of continuous stirring. The product obtained was then subjected to hydrothermal reaction by placing it in a preheated air oven for 24 h. The resultant product was washed three times with Milli-Q filtered water (resistivity ~ 18 MΩ cm) and rinsed once with ethanol, followed by drying in air at 70 °C for 24 h. The obtained Ln-241 was calcined under flowing H_2 (200 mL min^{-1}) at 1200 °C for 1 h to yield Ln_2O_2S and in ambient air (in Ar for the Tb and Pr analogues to prevent possible oxidation) at 1000 °C for 1 h to afford $Ln_2O_2SO_4$. The heating rate is 5 °C min^{-1} in the ramp stage of calcinations. $(Gd,RE)_2O_2S$ and $(Gd,RE)_2O_2SO_4$ phosphors (RE = 5 at% Eu or 1 at% Tb) were prepared as abovementioned.

Characterization

Phase characterization was performed *via* X-ray diffractometry (XRD; Model RIN T2200, Rigaku, Tokyo, Japan) operated at 40 kV/40 mA, using nickel-filtered Cu-Kα radiation (λ = 0.15406 nm). The XRD data for the Rietveld analysis were obtained in the step-scan mode with a step size of 0.02° and an accumulation time of 10 s. Rietveld refinement was carried out using the TOPAS 4.2 software.[30] The morphology of the products was observed *via* a field emission scanning electron microscope operated at 10 kV (FE-SEM; Model S-5000, Hitachi, Tokyo). Fourier transform infrared spectroscopy (FTIR; Model 4200, JASCO, Tokyo) was performed *via* the standard KBr pellet method. Thermogravimetric/differential thermal analyses (TG/DTA; Model STA449F3, Jupiter, NETZSCH, Germany) of the Ln-241 compounds were performed under flowing simulated air (50 mL min^{-1}) up to 1560 °C at the heating rate of 10 °C min^{-1}. The elemental composition of the products was also determined: for Ln, *via* inductively coupled plasma spectroscopy (ICP; Model IRIS Advantage, Jarrell-Ash Japan, Kyoto, Japan); for N, *via* spectrophotometry (Ubest-35, Japan Spectroscopic Co., Ltd, Tokyo); and for C and S, *via* combustion-infrared absorptiometry (Model CS-444LS, LECO, St. Joseph, MI). Photoluminescence spectra of the $(Gd,RE)_2O_2SO_4$ and $(Gd,RE)_2O_2S$ phosphors were obtained using an FP-6500 (JASCO) fluorescence spectrophotometer equipped with a 150 W xenon lamp for excitation at the scan speed of 100 nm min^{-1} and a slit width of 3 nm for both excitation and emission. The luminescence efficiency was determined using the absolute PL quantum yield (QY) measurement system (C9920-02, Hamamatsu Photonics K. K., Kanagawa, Japan). Cathodoluminescence of the $(Gd_{0.99}Tb_{0.01})_2O_2S$ green phosphor was measured by a spectroradiometer (HS-1000, Photal Otsuka Electronics, Osaka, Japan) in a vacuum chamber with a base pressure of 10^{-6} Pa at room temperature after the powder was deposited on a 1 × 1 cm^2 Al plate. The electron beam covered a circular area of 0.76 cm in diameter (~0.45 cm^2), from which the luminescence signal was obtained in the 300–800 nm region using a CCD camera. The

luminescence brightness (cd m^{-2}) was derived from the emission integrated over the wavelength region of measurement using a built-in software of the system.

Results and discussion

The effects of lanthanide contraction on the crystallization and extended synthesis of Ln-241 layered compound

Fig. 1 shows the XRD patterns of the products obtained *via* the hydrothermal reaction at 100 °C and pH = 9 for the entire lanthanide family (La–Lu). It can be seen that the La–Gd products conform well to the reported Ln-241 compounds,[1,31] whose phase purity and composition were further verified by the results of Rietveld refinements (Fig. S1†) and ICP analysis (Table S1†). The Ce product contains a CeO_2 impurity (indicated with an asterisk, ~28 wt%, detected by refinement) since Ce^{3+} is easily oxidized to Ce^{4+} in air at elevated temperatures, especially in an alkaline medium. The XRD peaks were indexed based on the results of Rietveld refinement, and the results are shown in Fig. 1 with La-241 as the reference. It was noticed that the (*h*00) diffraction peaks (such as (200)) only slightly shift towards the high-angle side with the decreasing ionic radius of Ln^{3+}, which is in sharp contrast to that observed for the non-(*h*00) peaks (such as (111)). This is due to the layered crystal structure and the peculiar crystalline nature of Ln-241 compounds, as has been discussed later. The diffraction patterns of the Tb–Ho compounds were indexed to the Ln-251 phase of $Ln_2(OH)_5(SO_4)_{0.5}\cdot nH_2O$,[32] and the presence of SO_4^{2-} instead of NO_3^- as the dominant interlayer anion was confirmed by the results of FTIR (Fig. S2†) and ICP (Table S1†) analysis. The (002) and (220) reflections of Ln-251 shift towards lower and higher angles with the decreasing size of Ln^{3+} due to the expanded interlayer distance and contracted *ab* plane of the crystal structure, respectively, as previously reported.[33] The XRD peaks of the Tm–Lu products cannot be indexed to any single phase according to the currently available standard diffraction files or reported references. However, both FTIR (Fig. S2†) and ICP (Table S1†) analyses suggest that they share high similarities with the Tb–Ho products in terms of chemical composition. The different XRD patterns may be mostly due to co-crystallization of high-hydration (HH) and low-hydration (LH) phases, as preliminarily analyzed in Fig. 1. The Er product exhibits an amorphous diffraction pattern, and appears to be a transition state between those of Ho and Tm.

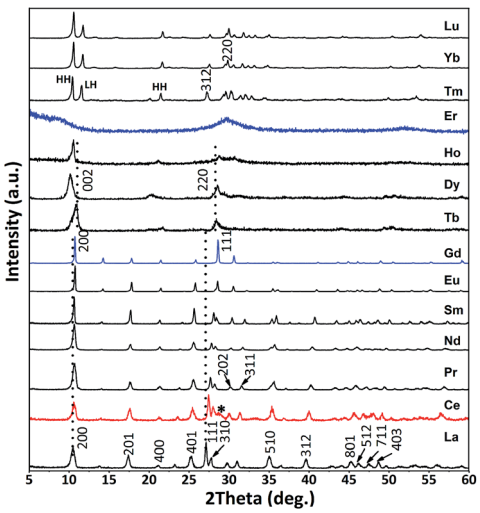

Fig. 1 XRD patterns of the products obtained *via* the hydrothermal reaction at 100 °C and pH = 9 for 24 h.

The abovementioned results unambiguously demonstrate the remarkable effect of Ln^{3+} size on the chemical composition and phase structure of the products. In the current reaction system, Ln^{3+} would undergo hydration and partial hydrolysis to form $[Ln(OH)_x(H_2O)_y(SO_4)_z]^{3-x-2z}$ complex ions.[34,35] The enhanced hydrolysis towards a smaller Ln^{3+}, driven by lanthanide contraction, would lead to a higher OH^-/Ln^{3+}, whereas a lower SO_4^{2-}/Ln^{3+} molar ratios, resulting in a phase transition from $Ln_2(OH)_4SO_4\cdot nH_2O$ (Ln = La–Gd) to $Ln_2(OH)_5(SO_4)_{0.5}\cdot nH_2O$ (Ln = Tb–Lu). Taking the abovementioned discussion into consideration, we lowered the solution pH to 7 and successfully obtained the Ln-241 compound for not only Tb^{3+} but also for the smaller Dy^{3+} ion (Fig. S3†). Rietveld refinements (Fig. 3a) revealed that the newly synthesized $Dy_2(OH)_4SO_4\cdot nH_2O$ has a monoclinic structure and is isostructural to its La–Tb counterparts (Fig. S1†). Note that efforts to obtain $Ln_2(OH)_4SO_4\cdot nH_2O$ for even smaller Ho–Lu ions failed even at pH = 7 although systematic experiments were performed in the wide temperature range of 100–200 °C. When the compounds with larger Ln ions such as La–Gd were synthesized at pH = 7 and 100 °C, it was found that they tend to crystallize as the less OH^--containing $Ln(OH)SO_4$ compound, and the pure Ln-241 phase was only obtained for Gd. These results further illustrate the effect of Ln^{3+} size on the hydrolysis and the importance of process conditions.

The products crystallized at 100 °C and pH = 9 show morphologies dependent on the type (ionic size) of Ln^{3+} (Fig. S4†). For the Ln-241 phase, it was observed that the La–Nd products consist of nanoplates (length up to ~1 μm), whereas Sm–Gd products consist of microplates (length up to ~50 μm). These results suggest a substantially lower nucleation density for the latter group. The Ln-251 compounds of Tb–Ho ($Ln_2(OH)_5(SO_4)_{0.5}\cdot nH_2O$) as well as the amorphous product of Er tend to be round particles although the extent of aggregation varies. The products of Ln = Tm–Lu also adopt plate-like morphologies although they are not the intended Ln-241 phase.

Fig. 2 shows the morphologies of the Ln-241 compounds obtained at 100 °C and pH = 7, where it can be seen that the particles are well dispersed and adopt spherical (for Gd, ~50 μm), peanut (for Tb, ~40 μm in length), and dumbbell (for Dy, up to ~130 μm in length) shapes. Closer observation (insets) revealed that the fundamental building blocks of these differently shaped particles are similar plate-like crystallites, conforming well to the layered structure of Ln-241. Upon comparing the SEM images of Gd-241 synthesized at pH = 7 (Fig. 2, spheres aggregated from plates) and pH = 9 (Fig. S4,† dispersed plates), it was obvious that solution pH significantly affects the particle morphology. The surfaces of the platelike primary crystallites of Ln-241 tend to be protonated in a neutral

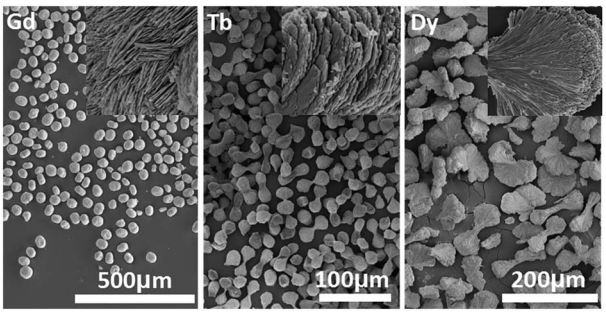

Fig. 2 SEM images of the $Ln_2(OH)_4SO_4 \cdot nH_2O$ products (Ln = Gd, Tb, and Dy) obtained *via* the hydrothermal reaction at 100 °C and pH = 7. The insets are the corresponding high resolution FESEM images.

or acidic solution, which attracts negatively charged SO_4^{2-} *via* electrostatic interaction and/or hydrogen bonding. As a result, the primary crystallites are glued together by the SO_4^{2-} groups to form the aggregates observed in Fig. 2. In an alkaline solution (pH = 9), the crystallite surface hardly contains any H^+, and the absence of the gluing effects of SO_4^{2-} may lead to dispersed plate-like crystallites, as observed in Fig. S4.†

Since Dy-241 is a new member of the Ln-241 family and its structural parameters have not been reported before, a detailed Rietveld refinement was carried out for this compound against its analogues (Fig. 3a), using the crystallographic data previously reported for La-241.[36] The main processing parameters and the refinement results are summarized in Table S2.† Clearly, all the X-ray diffractions of Dy-241 are well indexed to the monoclinic cell (*C*2/*m*) and the compound is isostructural to the already reported Ln = La–Tb counterparts, but with smaller

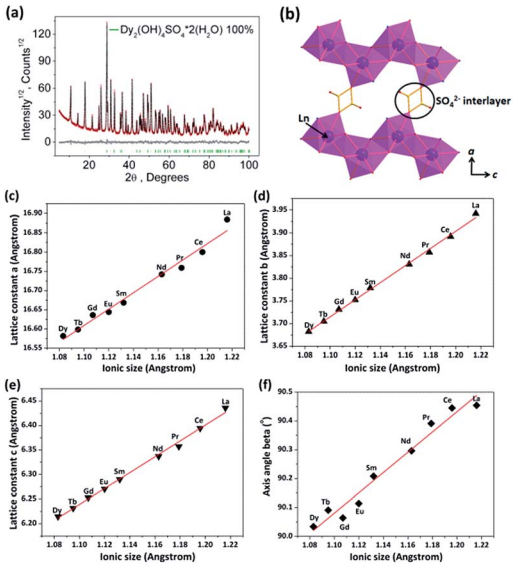

Fig. 3 (a) Observed (black) and calculated (red) XRD patterns and the difference (gray) for Dy-241, where the Bragg reflections are indicated with green tick marks; (b) illustration of the layered stacking pattern in the crystal structure of Dy-241; (c–e) correlation of lattice constants and (f) axis angle with the Ln^{3+} radius for the Ln-241 compound series (Ln = La–Dy). The ionic radius for the 9-fold coordinated Ln^{3+} is cited from ref. 37.

cell parameters and cell volume. The deduced lattice constants (*a*, *b*, and *c*) and axis angle (β) for the Ln = La–Dy series are shown in Fig. 3c–f and Table S3,† where it can be seen that the abovementioned structural parameters all monotonously decrease with the decreasing size of Ln^{3+}. The gallery height of Ln-241 is (a sin β)/2, and thus, the decreasing *a* constant also indicates a gradually contracting interlayer distance in the structure. It was also noticed that with a decrease in the ionic radius, from La^{3+} to Dy^{3+}, the *b* and *c* constants experienced a decrease of 6.6% and 3.4%, respectively, whereas a decrease of only 1.8% was observed for the *a* constant. The much smaller decrease in the *a* constant is primarily due to the constraining effects of the SO_4^{2-} interlayer (Fig. 3b) since the sulfate tetrahedron only shows a rather limited distortion in most crystal structures. This also agrees well with the sluggish shift of the (200) diffraction peaks, as observed in Fig. 1.

Thermal analysis, stability of $Ln_2O_2SO_4$, and green synthesis of Ln_2O_2S (Ln = La–Dy, except for Ce)

The thermal decomposition process of Ln-241 (Ln = La–Dy) was comparatively investigated *via* TG/DTA in the wide temperature range from RT to 1560 °C, and the results are shown in Fig. 4 for the two boundary compositions of La-241 and Dy-241 and in Fig. S5† for the rest. It was observed that the compounds similarly undergo dehydration (product: $Ln_2(OH)_2SO_4$), dehydroxylation (product: $Ln_2O_2SO_4$), and desulfuration (product: Ln_2O_3) at the increasingly higher temperatures, with each stage accompanied by an endotherm. The decomposition data are tabulated in Table 1 for the entire series, together with the number of water molecules (the *n* value, ~2) calculated from the first stage of decomposition. Clearly, the predicted (Table S4†) and observed (Table 1) weight losses agree well with each other, which supports the abovementioned decomposition procedures.

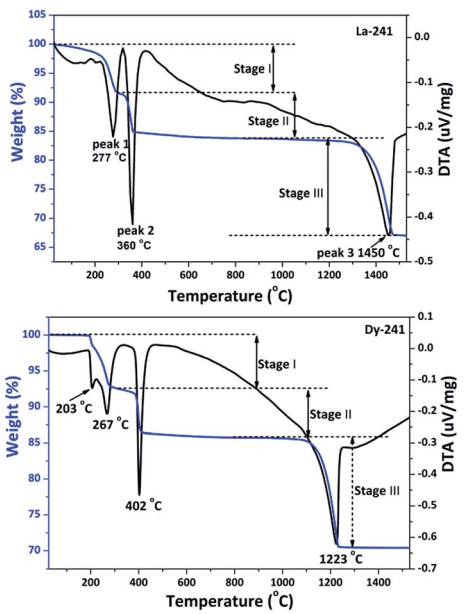

Fig. 4 TG/DTA curves for the La-241 and Dy-241 compounds.

Table 1 Thermal decomposition data for $Ln_2(OH)_4SO_4 \cdot nH_2O$ (Ln = La–Dy, except for Ce) in air

Ln	Peak 1 (°C)	Peak 2 (°C)	Peak 3 (°C)	Platform range	*n* value	Weight loss I (%)	Weight loss II (%)	Weight loss III (%)	Total weight loss (%)
La	277	360	1450	405–1300	2.20	8.24	7.92	16.78	32.94
Pr	276	352	1359	407–1220	2.37	8.76	8.30	16.47	33.53
Nd	274	353	1325	410–1180	2.31	8.56	7.79	16.14	32.49
Sm	272	363	1288	420–1150	2.17	7.76	7.38	15.78	30.92
Eu	269	371	1268	425–1130	2.16	7.69	7.19	15.64	30.52
Gd	265	387	1284	441–1120	2.16	7.57	7.05	15.96	30.58
Tb	267	396	1250	450–1110	2.15	7.43	7.27	15.59	30.29
Dy	267	402	1223	460–1080	2.02	6.92	7.16	15.42	29.50

It was noticed from Table 1 that the temperature of dehydroxylation (peak 2, removal of OH^-) tends to increase, whereas that of desulfuration (peak 3, removal of SO_4^{2-}) decreases as the Ln^{3+} size decreases. This leads to a gradually narrowed platform between the two peaks. It can thus be inferred that the stable temperature for $Ln_2O_2SO_4$ decreases for smaller Ln^{3+}, and $La_2O_2SO_4$ is the most stable amongst the $Ln_2O_2SO_4$ series of compounds. According to Pearson hard–soft–acid–base (HSAB) theory,[38,39] both OH^- and SO_4^{2-} are bases, whereas Ln^{3+} is an acid. The chemical hardness of OH^- and SO_4^{2-} is constant for the series, whereas the acid hardness of Ln^{3+} increases with the decreasing size of Ln^{3+} due to lanthanide contraction. As the hardness of OH^- is greater than that of SO_4^{2-}, the coordination of OH^- and SO_4^{2-} to Ln^{3+} becomes tighter and looser, respectively, as Ln goes from La to Lu, which leads to the observed gradually more difficult dehydroxylation and easier desulfuration. The dehydration (peak 1) temperature also tends to decrease as the Ln^{3+} size decreases, which may imply that the water molecules move towards an outer layer of the coordination sphere of Ln^{3+} or a looser coordination of H_2O to the Ln^{3+} center.

Calcining the Ln-241 compounds at 1000 °C for 1 h produced phase-pure $Ln_2O_2SO_4$ with a monoclinic structure (Ln = La–Dy, except for Ce), whose XRD patterns are shown in Fig. 5. The diffraction peaks clearly drift towards higher angles as the Ln^{3+} size decreases, indicating a contracted unit cell in the structure. The derived lattice constants, cell volume, and axis angle are summarized in Table S5.† Upon observation of the morphology (Fig. S6†), it was found that $La_2O_2SO_4$ is comprised of round particles disintegrated from La-241 nanoplates (Fig. S4†); $Pr_2O_2SO_4$ and $Nd_2O_2SO_4$ tend to preserve the plate-like morphologies of their precursors (Fig. S4†) although partial disintegration is evident, whereas the Sm–Dy oxysulfates fully inherit the morphology of their precursors (Fig. S4† and Fig. 2).

Fig. 6 exhibits the XRD patterns of the products obtained by calcination of Ln-241 under flowing H_2 at 1200 °C for 1 h. The diffraction peaks can be indexed to a pure or nearly pure phase of Ln_2O_2S with hexagonal structure. The trace amount of oxide impurity (indicated with an asterisk), observed in the Tb (~6 wt%) and Dy (~8 wt%) products, might be due to an insufficient reducing power of H_2 and/or lower thermal stability of $Tb_2O_2SO_4$ and $Dy_2O_2SO_4$ (Table 1). The synthetic approach for Ln_2O_2S does not involve any toxic sulfurizing reagent and has water vapor as the only exhaust, thus showing clear advantages over previous procedures.[26,27,40,41] The diffraction peaks steadily shift to higher angles as the Ln^{3+} size decreases, which is in agreement with the decreasing lattice constants and cell volume, as shown in Table S6.† The resultant Ln_2O_2S particles (Fig. S7†) tend to adopt the morphologies observed for $Ln_2O_2SO_4$, and the primary particles of the Sm–Dy products become significantly porous upon desulfuration (inset of Fig. S7†).

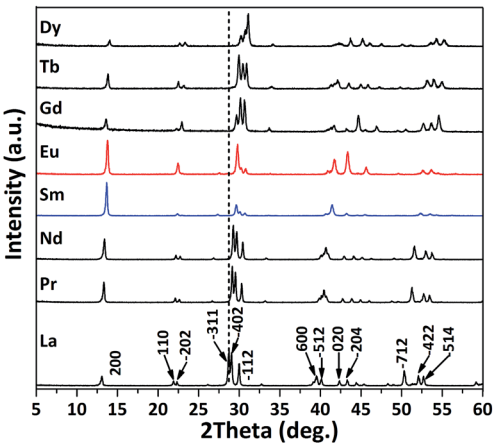

Fig. 5 XRD patterns of the $Ln_2O_2SO_4$ products obtained by the calcination of $Ln_2(OH)_4SO_4 \cdot nH_2O$ (Ln-241) at 1000 °C for 1 h in air (Ar for Tb-241 and Pr-241).

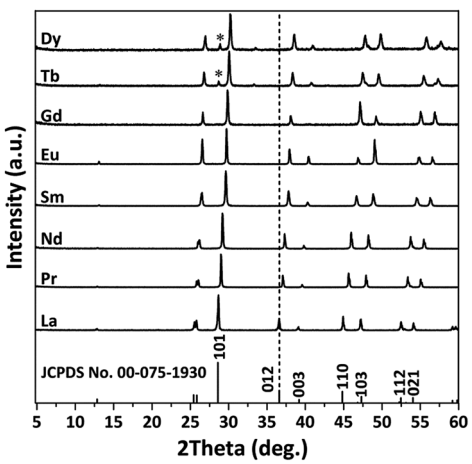

Fig. 6 XRD patterns of the products obtained by the calcination of $Ln_2(OH)_4SO_4 \cdot nH_2O$ under flowing H_2 at 1200 °C for 1 h.

Photoluminescence measurements for the $(Gd,RE)_2O_2S$ and $(Gd,RE)_2O_2SO_4$ phosphors (RE = Eu or Tb)

By the abovementioned hydrothermal strategy, $Gd_2(OH)_4SO_4 \cdot nH_2O$ (Gd-241) separately doped with 5 at% of Eu^{3+} ($(Gd_{0.95}Eu_{0.05})$-241) and 1 at% of Tb^{3+} ($(Gd_{0.99}Tb_{0.01})$-241) was successfully crystallized at 100 °C and at pH = 7 (Fig. S8†), which yielded phase-pure $(Gd,RE)_2O_2SO_4$ and $(Gd,RE)_2O_2S$ phosphors by calcination at 1000 °C in air (Ar for $(Gd_{0.99}Tb_{0.01})$-241) and at 1200 °C in H_2, respectively (Fig. S8†). The structural parameters of these materials are summarized in Table S7.† Neither Eu- nor Tb-doping appreciably affected the particle morphology of the product, as observed in Fig. S6† ($Gd_2O_2SO_4$) and Fig. S7† (Gd_2O_2S) and those shown in Fig. 7 for the Eu^{3+}-doped products.

Fig. 8 shows the PLE and PL spectra of Eu^{3+}- and Tb^{3+}-doped $Gd_2O_2SO_4$ and Gd_2O_2S, with the electronic transitions assigned in the figures. The excitation spectrum of Eu^{3+} in $Gd_2O_2SO_4$ (λ_{em} = 618 nm, Fig. 8a) presents a strong band centered at 277 nm in the 200–350 nm region and weaker intra-$4f^6$ transitions at longer wavelengths in the range of 350–500 nm. The $^8S_{7/2} \rightarrow {}^6I_J$ transition of Gd^{3+} is mostly observed at 275 nm in many hosts,[42–44] and thus, the 277 nm band may be resulted from overlapping of the $^8S_{7/2} \rightarrow {}^6I_J$ transition band of Gd^{3+} with the $O^{2-} \rightarrow Eu^{3+}$ charge transfer band. Under 277 nm excitation, the typical $^5D_0 \rightarrow {}^7F_J$ (J = 1–4) transitions of Eu^{3+} were observed in the 500–800 nm region, with the $^5D_0 \rightarrow {}^7F_2$ emission at 618 nm being predominant. On the other hand, the excitation spectrum of Eu^{3+} in Gd_2O_2S (λ_{em} = 625 nm, Fig. 8b) is characterized by a strong and broad band in the ~200–400 nm region that is composed of $O^{2-} \rightarrow Eu^{3+}$ charge transfer (peaked at ~265 nm), the $^8S_{7/2} \rightarrow {}^6I_J$ transition of Gd^{3+} (at ~277 nm), and the $S^{2-} \rightarrow Eu^{3+}$ charge transfer (at ~342 nm). Exciting the phosphor at 342 nm similarly leads to $^5D_0 \rightarrow {}^7F_J$ Eu^{3+} transitions, with the $^5D_0 \rightarrow {}^7F_2$ emission at ~625 nm being the strongest. The Eu^{3+} ions in $Gd_2O_2SO_4$ and Gd_2O_2S present the low-site C_1 and C_{3v} symmetries, respectively, and thus a stronger electric dipole $^5D_0 \rightarrow {}^7F_2$ transition than magnetic dipole $^5D_0 \rightarrow {}^7F_1$ transition was observed for both the cases.[21,45]

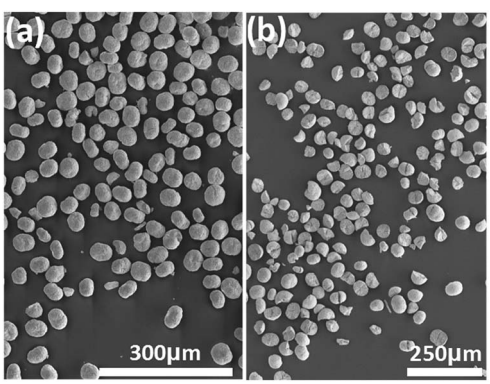

Fig. 7 FESEM images showing the particle morphologies of the resultant $(Gd_{0.95}Eu_{0.05})_2O_2SO_4$ (a) and $(Gd_{0.95}Eu_{0.05})_2O_2S$ (b) phosphors.

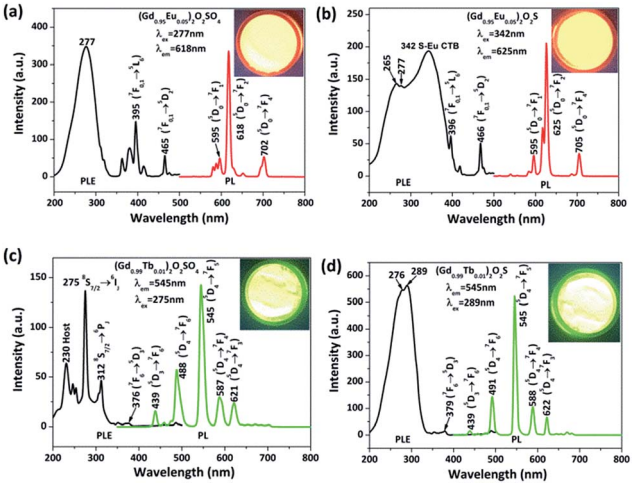

Fig. 8 PLE and PL spectra of the $(Gd,RE)_2O_2SO_4$ and $(Gd,RE)_2O_2S$ phosphors (RE = Eu or Tb). The inset shows the appearance of luminescence under UV irradiation of the corresponding phosphor from a hand-held UV lamp (365 nm for $(Gd_{0.95}Eu_{0.05})_2O_2S$ and 254 nm for the rest).

The PLE spectrum of $(Gd_{0.99}Tb_{0.01})_2O_2SO_4$ (λ_{em} = 545 nm, Fig. 8c) presents several sharp peaks in the ~200–325 nm region, with the $^8S_{7/2} \rightarrow {}^6I_J$ transition of Gd^{3+} at 275 nm being the strongest. The peak at 230 nm is due to host absorption.[36] Under 275 nm excitation, the $^5D_{3,4} \rightarrow {}^7F_J$ (J = 3–6) emissions of Tb^{3+}, with the green one at 545 nm being the strongest, were observed, indicating an efficient energy transfer from Gd^{3+} to Tb^{3+}. A distinctly different PLE spectrum was produced for Tb^{3+} in Gd_2O_2S for the same monitoring wavelength of 545 nm, which displayed a strong and broad band in the 200–340 nm region (peaked at 289 nm) that is resulted from overlapping of $^8S_{7/2} \rightarrow {}^6I_J$ Gd^{3+} transition with $4f^8 \rightarrow 4f^75d^1$ inter-configurational Tb^{3+}.[46,47] Exciting the phosphor at 289 nm produced a PL profile similar to that of $(Gd_{0.99}Tb_{0.01})_2O_2SO_4$ (Fig. 8d). The Eu^{3+}- and Tb^{3+}-doped phosphors have quantum yields of ~21–42% for different compositions, as shown in Table 2.

The fluorescence decay for both Eu^{3+} and Tb^{3+} in $Gd_2O_2SO_4$ and Gd_2O_2S was found to follow a single exponential mode in each case (Fig. S9†), and the derived lifetime values are displayed in Table 2. Generally, shorter lifetimes were observed for Gd_2O_2S with both Eu^{3+} and Tb^{3+}. No lifetime data are available for $(Gd,Tb)_2O_2SO_4$ for a direct comparison, but the lifetimes determined in this study for $(Gd,Eu)_2O_2SO_4$ (1.41 ms), $(Gd,Eu)_2O_2S$ (0.80 ms), and $(Gd,Tb)_2O_2S$ (1.27 ms) are in reasonable agreement with the reported values of 1.31–1.86 ms for $(Gd,Eu)_2O_2SO_4$ and $(Y,Eu)_2O_2SO_4$,[48,49] 0.66–0.92 ms for $(Gd,Eu)_2O_2S$ and $(Y,Eu)_2O_2S$,[50,51] and 0.78–1.10 ms for $(Gd,Tb)_2O_2S$ and $(La,Tb)_2O_2S$.[51,52] The CIE color coordinates derived from the PL spectra are shown in Table 2 and Fig. S10,† where it can be seen that Tb^{3+} and Eu^{3+} ions in Gd_2O_2S have more green and red components, respectively. Table 2 also shows that $(Gd,RE)_2O_2SO_4$ has a generally smaller crystallite size than $(Gd,RE)_2O_2S$ owing to its lower temperature of calcination.

Table 2 Optical properties and crystallite sizes of the $(Gd,RE)_2O_2SO_4$ and $(Gd,RE)_2O_2S$ phosphors

Samples	Lifetime (ms)	CIE (x, y)	Crystallite size (nm)	Quantum yield (%)
$(Gd_{0.95}Eu_{0.05})_2O_2SO_4$	1.41 (0.01)	(0.657, 0.343)	43	28.6
$(Gd_{0.95}Eu_{0.05})_2O_2S$	0.80 (0.01)	(0.669, 0.330)	55	20.6
$(Gd_{0.99}Tb_{0.01})_2O_2SO_4$	2.25 (0.01)	(0.327, 0.519)	38	21.5
$(Gd_{0.99}Tb_{0.01})_2O_2S$	1.27 (0.01)	(0.329, 0.569)	57	42.0

Cathodoluminescence (CL) properties of the $(Gd,Tb)_2O_2S$ green phosphor

Fig. 9 shows the cathodoluminescence (CL) spectrum of the $(Gd_{0.99}Tb_{0.01})_2O_2S$ green phosphor. The emission spectrum (Fig. 9a) obtained under a constant electron-beam current of 25 μA is similar to the PL emission spectrum displayed in Fig. 8d. The emission intensity improved as the acceleration voltage increased and the color coordinates were almost constant, which indicates a good luminescence stability for the phosphor. For cathodoluminescence measurements, the activators are excited by the plasma produced by the incident electrons. A higher beam current will generate more plasma, and hence, an enhanced emission brightness was observed upon increasing beam current under a fixed acceleration voltage of 3 kV (Fig. 9b). On the other hand, electron energy increases with the increasing acceleration voltage, allowing the electrons to penetrate deeper into the phosphor particles, which leads to an increased electron–solid interaction and thus improved CL brightness of the phosphor under a fixed current of 25 μA (Fig. 9c). The electron penetration depth can be correlated to the acceleration voltage and material properties by the following equations:[53,54]

$$L\ [\text{Å}] = 250(A/\rho)(E/Z^{1/2})^n \quad (1)$$

$$N = 1.2/(1 - 0.29\ \log_{10} Z) \quad (2)$$

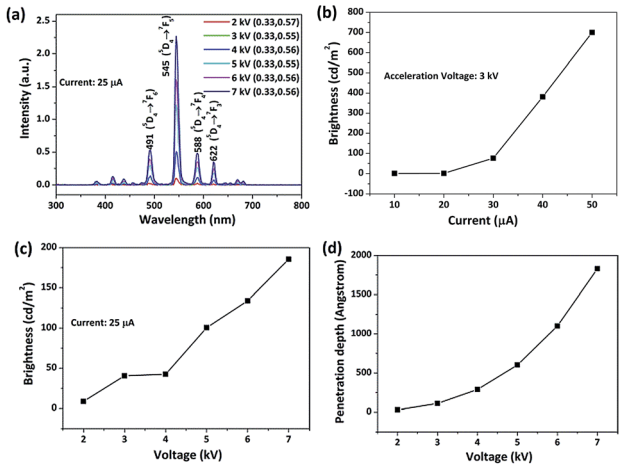

Fig. 9 (a) Cathodoluminescence spectrum of the $(Gd_{0.99}Tb_{0.01})_2O_2S$ green phosphor, obtained under a fixed electron beam current of 25 μA; brightness of emission *versus* (b) irradiation current and (c) acceleration voltage; and (d) calculated penetration depth as a function of the acceleration voltage.

where A is the atomic or molecular weight of the compound, ρ is the bulk density, Z is the atomic number per molecule in the material, and E is the acceleration voltage (kV). In this study, $Z = 160$, $A = 378.53$, and $\rho = 7.34$ g cm^{-3}. The calculation results are displayed in Fig. 9d, where it can be seen that the penetration depth continuously increases from ~29 to 1830 Å as the acceleration voltage increases from 2 to 7 kV.

Conclusions

The layered sulfate-based $Ln_2(OH)_4SO_4 \cdot nH_2O$ hydroxide (Ln-241) was systematically studied in terms of hydrothermal synthesis conditions, crystal structure, and thermal behaviour, and the effect of lanthanide contraction was revealed. It was also shown that Ln-241 can be facilely transformed into the two important groups of $Ln_2O_2SO_4$ and Ln_2O_2S compounds *via* water removal for potential applications including luminescence. The main conclusions are summarized as follows:

(1) the hydrothermal product transforms from $Ln_2(OH)_4SO_4 \cdot nH_2O$ (Ln = La–Gd) to $Ln_2(OH)_5(SO_4)_{0.5} \cdot nH_2O$ (Ln = Tb–Lu) with the decreasing ionic size of Ln at 100 °C and pH = 9. Lowering the solution pH to 7 allows the crystallization of pure Ln-241 for the smaller Dy^{3+} ion, thus extending the Ln-241 family of compounds. The decrease in the Ln^{3+} size leads to increasingly smaller lattice parameters (a, b, and c), cell volume, and axis angle across the Ln series (La–Dy).

(2) $Ln_2(OH)_4SO_4 \cdot nH_2O$ shows three steps of weight loss upon heating in air that correspond to dehydration, dehydroxylation, and desulfurization. The temperature of the 2nd stage tends to increase, whereas those of the 1st and 3rd stages tend to decrease as the Ln^{3+} size decreases. As a result, the stable temperature range for $Ln_2O_2SO_4$ narrows as the Ln^{3+} size decreases. Calcining the Ln-241 compounds in air at 1000 °C and in H_2 at 1200 °C produces $Ln_2O_2SO_4$ and Ln_2O_2S, respectively, with water vapour as the only exhaust.

(3) The Eu^{3+} and Tb^{3+} activators in $Gd_2O_2SO_4$ and Gd_2O_2S produce red and green emissions, respectively, due to their characteristic f–f transitions under UV excitation, and the effect of the host lattice was revealed in terms of excitation, emission, fluorescence decay, quantum yield, and emission color. Through cathodoluminescence measurements, it was found that $(Gd_{0.99}Tb_{0.01})_2O_2S$ is stable in the studied range and exhibits an increasingly higher emission brightness on increasing either the acceleration voltage (up to 7 kV) or the electron beam current (up to 50 μA).

Acknowledgements

This work was partly supported by the National Natural Science Foundation of China (Grants No. 51672039, 51172038, and 51302032), the Fundamental Research Fund for the Central Universities (Grant No. N140204002), the Grants-in-Aid for Scientific Research (KAKENHI No. 26420686), and the Russian Foundation for Basic Research (15-52-53080). Xuejiao Wang acknowledges the financial support received from the China Scholarship Council for her overseas Ph. D. study at the National Institute of Materials Science (Contract No. 201406080035).

Notes and references

1 J. B. Liang, R. Z. Ma, F. X. Geng, Y. Ebina and T. Sasaki, *Chem. Mater.*, 2010, **22**, 6001.
2 J. B. Liang, R. Z. Ma and T. Sasaki, Photofunctional Layered Materials, *Struct. Bonding*, 2015, **166**, 69.
3 X. L. Wu, J.-G. Li, Q. Zhu, W. G. Liu, J. Li, X. D. Li, X. D. Sun and Y. Sakka, *J. Mater. Chem. C*, 2015, **3**, 3428.
4 F. X. Geng, Y. Matsushita, R. Z. Ma, H. Xin, M. Tanaka, F. Izumi, N. Iyi and T. Sasaki, *J. Am. Chem. Soc.*, 2008, **130**, 16344.
5 K.-H. Lee, B. I. Lee, J. H. You and S. H. Byeon, *Chem. Commun.*, 2010, **46**, 1461.
6 L. J. McIntyre, L. K. Jackson and A. M. Fogg, *J. Phys. Chem. Solids*, 2008, **69**, 1070.
7 H. J. Jeong, B.-I. Lee and S.-H. Byeon, *ACS Appl. Mater. Interfaces*, 2016, **8**, 10946.
8 F. X. Geng, R. Z. Ma, Y. Matsushita, J. B. Liang, Y. Michiue and T. Sasaki, *Inorg. Chem.*, 2011, **50**, 6667.
9 J. H. Wu, J. B. Liang, R. Z. Ma and T. Sasaki, *J. Phys. Chem. C*, 2015, **119**, 26229.
10 G. Ferru, B. Reinhart, M. K. Bera, M. O. de la Cruz, B. F. Qiao and R. J. Ellis, *Chem.–Eur. J.*, 2016, **22**, 6899.
11 M. Seitz, A. G. Oliver and K. N. Raymond, *J. Am. Chem. Soc.*, 2007, **129**, 11153.
12 D. J. Zhang, F. Yoshioka, K. Ikeue and M. Machida, *Chem. Mater.*, 2008, **20**, 6697.
13 J. D. Lessard, I. Valsamakis and S. M. Flytzani, *Chem. Commun.*, 2012, **48**, 4857.
14 I. Valsamakis and M. Flytzani-Stephanopoulos, *Appl. Catal., B*, 2011, **106**, 255.
15 S. Yamamoto, S. Tamura and N. Imanaka, *J. Alloys Compd.*, 2006, **418**, 226.
16 T. Yang, A. L. Shaula, S. M. Mikhalev, D. Ramasamy and D. P. Fagg, *J. Power Sources*, 2016, **306**, 611.
17 J. B. Lian, X. D. Sun, Z. G. Liu, J. Y. Yu and X. D. Li, *Mater. Res. Bull.*, 2009, **44**, 1822.
18 F. S. Chen, G. Chen, T. Liu, N. Zhang, X. H. Liu, H. M. Luo, J. H. Li, L. M. Chen, R. Z. Ma and G. Z. Qiu, *Sci. Rep.*, 2015, **5**, 17934.
19 J. W. Haynes and J. J. Brown Jr, *J. Electrochem. Soc.*, 1968, **115**, 1060.
20 M. Shoji and K. Sakurai, *J. Alloys Compd.*, 2006, **426**, 244.
21 X. J. Wang, J.-G. Li, Q. Zhu and X. D. Sun, *J. Mater. Res.*, 2016, **31**, 2268.
22 S. David, C. Michail, I. Seferis, I. Valais, G. Fountos, P. Liaparinos, I. Kandarakis and N. Kalyvas, *J. Lumin.*, 2016, **169**, 706.
23 J. Liu, H. D. Luo, P. J. Liu, L. X. Han, X. Zheng, B. Xu and X. B. Yu, *Dalton Trans.*, 2012, **41**, 13984.
24 S. A. Osseni, S. Lechevallier, M. Verelst, *et al.*, *Nanoscale*, 2014, **6**, 555.
25 H. Mass, Penetration phosphors for display devices, *US Pat.*, 4,105,909, Sperry Rand Corporation, 1978.
26 C. R. Ronda, G. Zeitler, H. Schreinemacher, N. Conrads and D. U. Wiechert, Gd_2O_2S material for use in CT applications, *US Pat.*, US 2011/0114887 A1, Koninklijke Phillips Electronics, N. V., Eindhoven, NL, 2011.
27 D. K. Nath and M. Ohio, Preparation of rare earth oxysulfide luminescent materials, *US Pat.*, 3856698, General Electric Company, 1974.
28 S.-H. Yu, Z.-H. Han, J. Yang, H.-Q. Zhao, R.-Y. Yang, Y. Xie, Y.-T. Qian and Y.-H. Zhang, *Chem. Mater.*, 1999, **11**, 192.
29 Y. Kawahara, V. Petrykin, T. Ichihara, N. Kijima and M. Kakihana, *Chem. Mater.*, 2006, **18**, 6303.
30 *TOPAS V4.2: General profile and structure analysis software for powder diffraction data—User's Manual*, Bruker AXS, Karlsruhe, Germany, 2008.
31 X. J. Wang, J.-G. Li, Q. Zhu, X. D. Li, X. D. Sun and Y. Sakka, *Sci. Technol. Adv. Mater.*, 2014, **15**, 014204.
32 X. J. Wang, J.-G. Li, Q. Zhu and X. D. Sun, *J. Am. Ceram. Soc.*, 2015, **98**, 3236.
33 X. L. Wu, J.-G. Li, Q. Zhu, J. K. Li, R. Z. Ma, T. Sasaki, X. D. Li, X. D. Sun and Y. Sakka, *Dalton Trans.*, 2012, **41**, 1854.
34 L. C. Thompson, Complexes, in *Handbook on the Physics and Chemistry of Rare Earths*, ed. K. A. Gschneidner Jr and L. Eyring, North-Holland Physics, Amsterdam, 1979.
35 E. N. Rizkalla and G. R. Choppin, *J. Alloys Compd.*, 1992, **180**, 325.
36 X. J. Wang, J.-G. Li, M. S. Molokeev, Q. Zhu, X. D. Li and X. D. Sun, *Chem. Eng. J.*, 2016, **302**, 577.
37 R. D. Shannon, *Acta Crystallogr., Sect. A: Cryst. Phys., Diffr., Theor. Gen. Crystallogr.*, 1976, **32**, 751.
38 R. G. Pearson, *J. Am. Chem. Soc.*, 1963, **85**, 3533.
39 P. R. Chinnam, R. N. Clymer, A. A. Jalil, S. L. Wunder and M. J. Zdilla, *Chem. Mater.*, 2015, **27**, 5479.
40 S.-H. Yu, Z.-H. Han, J. Yang, H.-Q. Zhao, R.-Y. Yang, Y. Xie, Y.-T. Qian and Y.-H. Zhang, *Chem. Mater.*, 1999, **11**, 192.
41 Y. Kawahara, V. Petrykin, T. Ichihara, N. Kijima and M. Kakihana, *Chem. Mater.*, 2006, **18**, 6303.
42 J. K. Li, J.-G. Li, S. H. Liu, X. D. Li, X. D. Sun and Y. Sakka, *J. Mater. Chem. C*, 2013, **1**, 7614.
43 H. X. Guan, G. X. Liu, J. X. Wang, X. T. Dong and W. S. Yu, *New J. Chem.*, 2014, **38**, 4901.
44 X. M. Zhang, F. G. Meng, W. L. Li, S. I. Kim, Y. M. Yu and H. J. Seo, *J. Alloys Compd.*, 2013, **578**, 72.
45 A. S. Souza and M. A. Couto Dos Santos, *Chem. Phys. Lett.*, 2012, **521**, 138.
46 P. Dorenbos, *J. Lumin.*, 2000, **91**, 91.
47 S. Mukherjee, V. Sudarsan, R. K. Vatsa, S. V. Godbole, R. M. Kadam, U. M. Bhatta and A. K. Tyagi, *Nanotechnology*, 2008, **19**, 325704.

48 T. Kijima, T. Shinbori, M. Sekita, M. Uota and G. Sakai, *J. Lumin.*, 2008, **128**, 311.
49 J. B. Lian, X. D. Sun, Z. G. Liu, J. Y. Yu and X. D. Li, *Mater. Res. Bull.*, 2009, **44**, 1822.
50 L. Han, M. M. Pan, Y. Lv, Y. T. Gu, X. F. Wang, D. Li, Q. L. Kong and X. T. Dong, *J. Mater. Sci.: Mater. Electron.*, 2015, **26**, 677.
51 Y. H. Song, H. P. You, Y. J. Huang, M. Yang, Y. H. Zheng, L. H. Zhang and N. Guo, *Inorg. Chem.*, 2010, **49**, 11499.
52 Z. G. Liu, X. D. Sun, S. K. Xu, J. B. Lian, X. D. Li, Z. M. Xiu, Q. Li, D. Huo and J.-G. Li, *J. Phys. Chem. C*, 2008, **112**, 2353.
53 C. He, Z. G. Xia and Q. L. Liu, *Opt. Mater.*, 2015, **42**, 11.
54 J.-G. Li, J. K. Li, Q. Zhu, X. J. Wang, X. D. Li, X. D. Sun and Y. Sakka, *RSC Adv.*, 2015, **5**, 59686.